

Analysis of converted refractions for shear statics and near-surface characterisation

Alan Meulenbroek¹ Steve Hearn^{1,2}

¹Velseis Pty Ltd and School of Earth Sciences, University of Queensland, PO Box 118, Sumner Park, QLD 4074, Australia.

²Corresponding author. Email: steveh@velseis.com

Abstract. Converted-wave refraction statics is an algorithm that incorporates both P-wave and S-wave refraction events to correct S-wave static errors in multicomponent seismic data. Conventional (PPP) and converted (PPS) refractions are picked on vertical and inline-horizontal shot records respectively. These picks are then analysed using the reciprocal method to create a near-surface model from which S-wave receiver statics are derived.

The derived PPS refraction statics have a similar short-wavelength character to S-wave statics obtained via statistical analysis of converted-wave reflections. Based on standard P-wave practice, we believe that an optimal production approach will include converted-refraction analysis, followed by converted-wave residual statics.

Although the thrust of this work has been towards derivation of S-wave statics, an interesting auxiliary output is also available. Based on theoretical modelling, the observed S-to-P time-depth ratios can be tuned to provide P-to-S velocity ratios (and hence dynamic Poisson's ratios) for the near-surface. This has interesting implications for lithological and rock strength analysis in mining, geotechnical and environmental investigations.

Key words: converted-wave, multi-component seismic, near-surface, refraction, shear-wave statics.

Introduction

In certain geological situations, a richer interpretation can be achieved through integrated compressional-wave (P-wave) and shear-wave (S-wave) seismic imaging. Converted-wave (or PS) reflection is an economical approach to such integrated analysis. However, one major impediment to viable onshore PS imagery relates to the difficulty in defining and processing S-wave receiver statics (e.g. Cary and Eaton, 1993). This is usually attributed to near-surface S velocities being lower, and often more variable, than P velocities.

Various approaches to solving S-wave statics have appeared in the literature in the past. These range from analysis of SSS refractions (S-wave from source to the refractor, along the refractor and back to the surface) (Schafer, 1991); analysis of common-receiver-point (CRP) stacks (Cary and Eaton, 1993) and analysis of PPS refractions (refracted waves which convert from P to S for the upgoing, head-wave section) (Houston et al., 1989). The converted-refraction technique discussed in this paper is conceptually related to the method of Houston et al. (1989), although the algorithmic approach is different. Our approach extends the standard reciprocal method (Hawkins, 1961), which is widely used in 2D P-wave refraction statics. The reciprocal method is closely related to earlier reversed-spread approaches presented by Hagiwara and Omote (1939) and Hagedoorn (1959).

To derive our S-wave receiver-statics solution, we apply the following processing flow:

1. Pick PPP and PPS arrivals and apply necessary adjustments so that pick timing is correct in an absolute sense. Because PPS refractions are not first arrivals, their identification and analysis is more challenging than for standard PPP refractions.
2. Perform reversed-spread refraction analysis to derive P- and S-wave time-depths and velocity functions. When reversed

refraction data are not available we incorporate the delay-time algorithm (Gardner, 1939).

3. Tune the S-to-P time-depth ratio to estimate the V_P/V_S ratio (γ) in the weathering layer.
4. With knowledge or estimation of V_P in the weathering layer, calculate V_S in the weathering layer, and the S-wave weathering static correction.

In order to perform this processing flow, well known refraction analysis techniques must be extended to accommodate converted refractions. The necessary extensions to conventional refraction theory are derived and discussed in a companion paper (Hearn and Meulenbroek, 2011). That paper provides additional detail regarding theory, terminology and practical application.

The particular dynamite dataset (referred to as ACARP Dataset #3) analysed in this paper was acquired at a site in the Bowen Basin which was chosen specifically by mine staff to be useful in illustrating lithological issues. The geology along the 2D line is known to exhibit lateral heterogeneity (Velseis, 2007).

Pre-processing and picking of refraction data

Identification and enhancement of refraction arrivals

S-wave signal-to-noise ratio (S/N) is generally weaker than P-wave S/N (e.g. Garotta et al., 2004). In order that the PPS refraction event can be picked, the S/N must be improved. Refracted arrivals often tend to have a lower dominant frequency than reflected arrivals. In such instances, the application of suitable filtering may help to clarify the recorded refracted waves (e.g. Vasil'ev, 1957). Here we use a zero-phase, high-cut filter to emphasise the lower frequencies associated with refractions, particularly PPS refractions, and to attenuate other sources of noise.

The low frequency character of the PPS refraction may impose some restrictions on the acquisition parameters which can be used. For example, one dataset considered in this project (ACARP Dataset #1) was recorded on geophones of natural frequency 40 Hz. On those data, we were not able to consistently identify a PPS refraction on the inline component shot records, even with extensive bandpass filtering. The geophones effectively act as a low-cut filter, restricting the usable bandwidth to frequencies greater than that of the PPS refraction.

The dataset to be discussed here (ACARP Dataset #3) is a 2D-3C dynamite line from the Bowen Basin in central Queensland. The natural frequency of the geophones is 14 Hz with 395 Ω coil resistance. For reference, Figure 1 shows the first 650 ms of a typical, unfiltered vertical component shot record. The PPP refraction event is indicated. As expected, the PPS refraction event is not obvious on the vertical component.

We were able to identify the PPS refraction event on the near offsets on the unfiltered inline component shot records (Figure 2). A band-pass filter assisted identification of the event (Figure 3), particularly on the far offsets. The event annotated in Figures 2 and 3 has been identified as the PPS refraction. First, the event is stronger on the inline component, suggesting it arrives at the geophone as an S wave. Second, it has approximately the same slope as the PPP refraction in Figure 1, indicating that the wave-

type along the refractor is the same. The PPS arrival is delayed in time (relative to the PPP refraction) due to the lower velocity of the upgoing S head-wave.

Polarity and absolute timing of refracted arrivals

In conventional refraction statics analysis, ‘picking’ is typically carried out on a convenient peak or trough close behind the true first arrival. The derived statics are correct in a relative sense. Technically, a small constant shift may still remain, but this is generally not significant in conventional processing.

Because we are aiming to use the ratio of the derived time-depths (t_{GS}/t_{GP}) to estimate V_P/V_S (γ) in the near surface, the absolute timing of the PPP and PPS refractions is more critical. For logistical convenience, we have picked both the PPP and PPS events on the first strong peak, using filtered records. As detailed below, this peak time then needs to be adjusted back to the true first break. As part of this adjustment, we have to know the expected polarity of the PPP and PPS refraction events. In order to determine this, we performed tap tests on the geophones used to record the 3C data. Our vertical geophones obey the normal convention, such that the PPP refraction should yield a negative break on the vertical component, since it provides an upward impact. In our case, the inline component geophone is oriented in the ground such that, for a geophone at positive offset, an impact towards the shot produces a positive break. (Note that this is the reverse of a proposed SEG convention for three-component geophone polarity (Brown et al., 2002).)

Intuitively, the converted S wave can be thought of as arising from the shearing motion caused on the refracting interface by the horizontally travelling compression and rarefaction. Thus for geophones at positive offsets, the first motion is away from the source (Figure 4). Hence, in our case, the true PPS arrival occurs at the first negative break before the peak on which that event was picked. For geophones at negative offsets, the shearing motion is also away from the source but in the opposite direction (Figure 4), causing the PPS event to produce a positive break on the shot record. The polarity of the trailing spread must be reversed in order for this event to have the same polarity on both leading and trailing spreads (e.g. Brown et al., 2002).

Based on the above logic, we can adjust the picks so that they are correct in an absolute sense. By experimentation, we found that a zero-phase bandpass filter will eliminate unwanted frequencies but will generally keep the centre of the

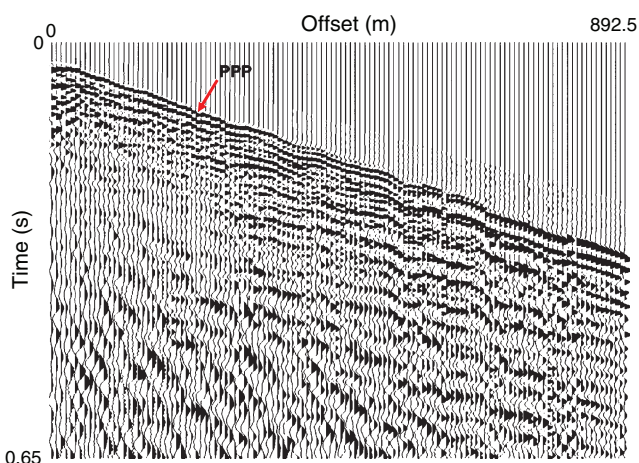


Fig. 1. Representative unfiltered vertical component shot record with the PPP refraction event indicated.

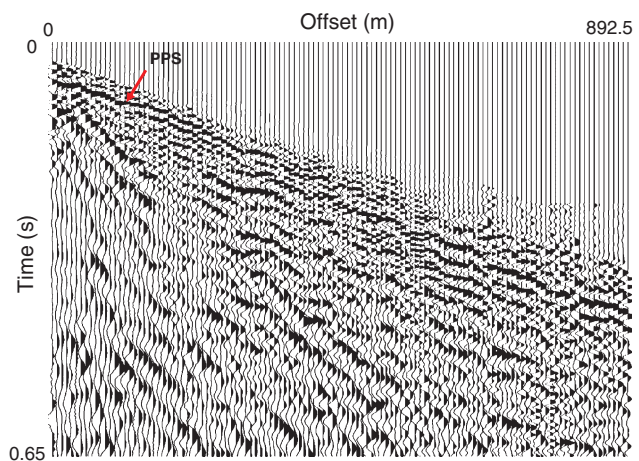


Fig. 2. Representative unfiltered inline component shot record with the PPS refraction event indicated.

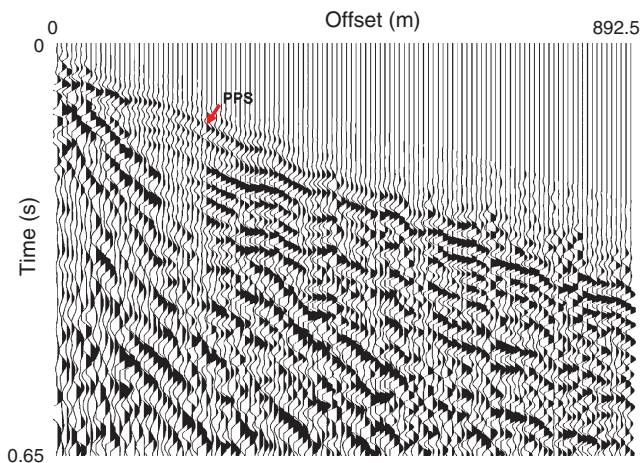


Fig. 3. Representative inline component shot record, with the PPS refraction event indicated. A zero phase bandpass filter (4, 8, 35, 60 Hz) has attenuated high-frequency noise, improving the coherence of the refraction event.

peak at approximately the same arrival time. This results in the broadening and smoothing of the wavelet as high frequencies are cut. Because of this, the true first-arrival time adjustment for the vertical and inline component data should be estimated using the unfiltered data. The adjustment to be applied is the time difference between the picked peak on the filtered shot record and the true first arrival on the unfiltered shot record. For our vertical component PPP refractions, this adjustment is -8 ms, i.e. the true PPP onset (measured on the unfiltered data) occurs, on average, 8 ms before the picked peak (measured on the filtered data). For the inline component PPS refractions, this adjustment is, on average, -12 ms. Note, that for this dataset, a constant time correction has proven sufficient. In other cases, it may be necessary to use an offset-dependent time correction.

PPP and PPS refraction picks

Figure 5 shows the PPP (vertical) refraction picks obtained from the ACARP #3 data. There is good coverage on both forward and reverse spreads from which to perform reciprocal analysis. Figure 6 shows the PPS (inline) refraction picks obtained from the ACARP #3 data. As expected, the PPS pick times are later than the PPP pick times. In contrast to the vertical component data, there is a lack of picks between Stations 200 and 275 due to difficulty in identifying the PPS refraction. Possible explanations for this include severe statics (caused by lateral heterogeneity) or low PPS amplitudes (caused by fundamental rock properties or anelastic attenuation). We are currently researching the influence of rock properties on refraction amplitudes.

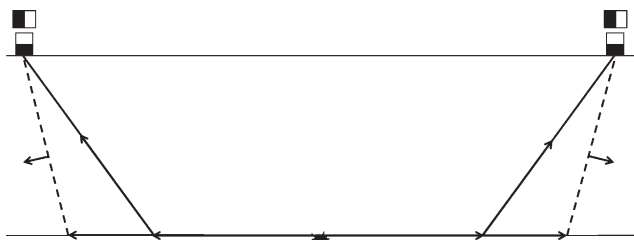


Fig. 4. Polarity of first motion for PPP and PPS refractions from an explosive source. Solid and dashed lines represent P-wave and S-wave segments respectively. The PPP refraction produces an upward particle motion at both positive and negative offsets. The PPS refraction produces a particle motion towards the right for positive offsets, and towards the left for negative offsets.

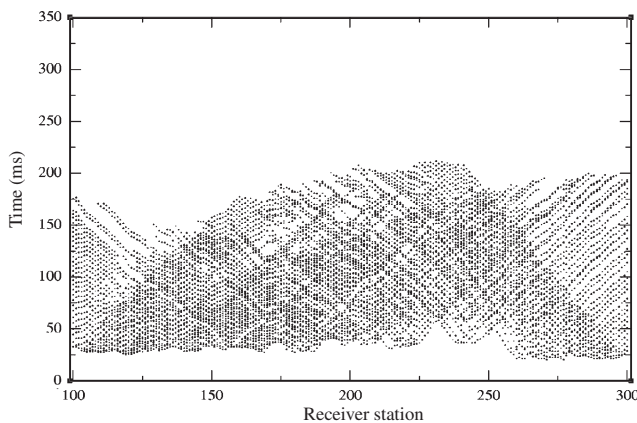


Fig. 5. Forward and reverse PPP refraction arrival times, picked from vertical component data.

Reversed-spread refraction analysis

Construction of composite spread

After we have picked the refraction data, the next step is to perform the reversed-spread refraction analysis. Here we have used a composite-spread approach, whereby single forward and reverse spreads are constructed using a production algorithm described by Hearn and Stanley (1983). This algorithm works by shifting the refraction picks from each shot point progressively later in time. The shifts are derived empirically by estimating the average time differences between refraction arrivals from adjacent shot-points. Figures 7 and 8 show the PPP and PPS refraction picks after this ‘compositing’ process. Consistent with the preceding discussion, the PPS composite exhibits greater scatter at each station, and discontinuities in zones where no picks are available. These composite curves are then averaged in time at each receiver station to yield the composite refraction spreads seen in Figures 9 and 10, which provide input for the reciprocal method.

The composite spread approach used here has some advantages over other approaches to the integration of multiple-shot refraction data (e.g. averaging at the time-depth stage). Because averaging takes place at the raw pick stage (rather than, for example, at the time-depth stage) it is relatively easy to detect and remove bad picks. This provides improved potential for retention of short-wavelength static features. Additionally, time errors caused by picking on the

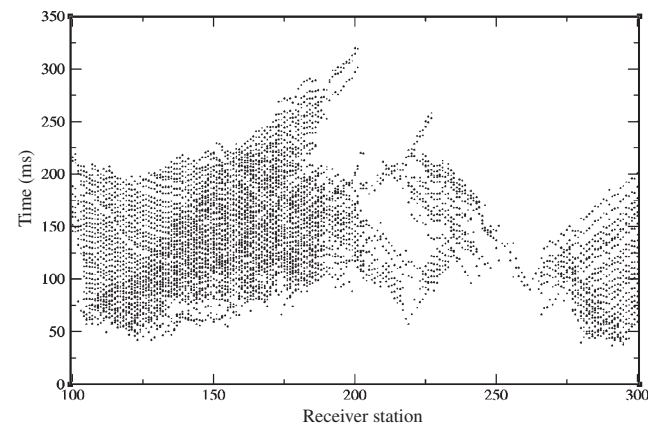


Fig. 6. Forward and reverse PPS refraction arrival times, picked from inline component data. PPS refractions exhibited poor quality in the region between Stations 200 and 270, resulting in fewer usable picks.

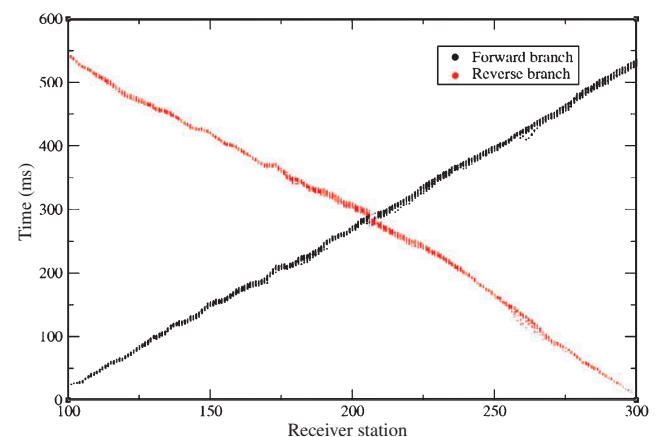


Fig. 7. PPP refraction picks after the compositing process.

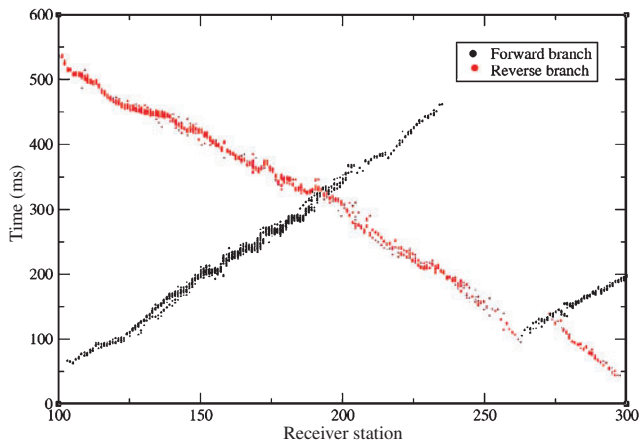


Fig. 8. PPS refraction picks after the compositing process. The compositing process is ‘reset’ when refraction times from adjacent shot points do not share any common receiver station (e.g. around Station 235 on forward branch, and Station 270 on reverse branch).

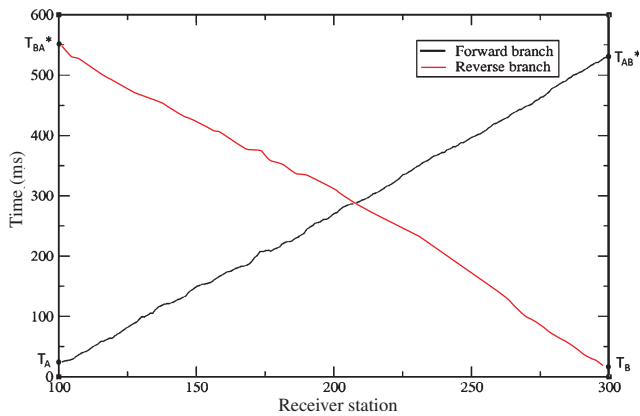


Fig. 9. Composite PPP refraction curves, averaged in time at each receiver station. The intercept times used in the buried shot correction are indicated. (See Figure 9 of Hearn and Meulenbroek, 2011).

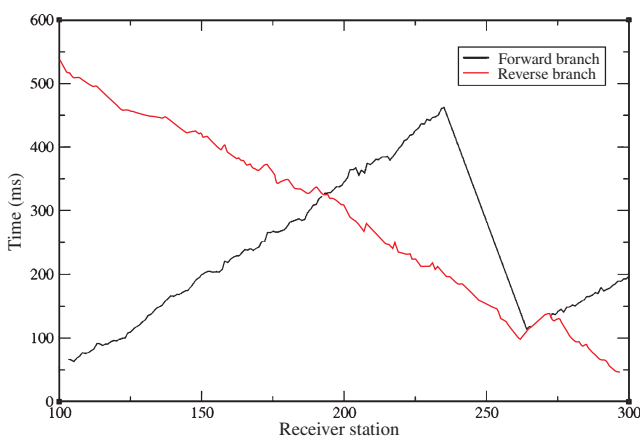


Fig. 10. Composite PPS refraction curves, averaged in time at each receiver station. The discontinuities are as discussed in the Figure 7 caption, and in the text.

wrong cycle are automatically corrected in the pick shifting process.

On the negative side, the shifting process can introduce long-wavelength ‘drift’ into the composite curve, and hence into the

derived statics. In order to reduce this effect, we recognise that any accumulating error in the composite curve will also accumulate into the reciprocal time. Hence when computing time depths, we use a laterally-varying reciprocal time, such that the drift error tends to be removed when the reciprocal time is subtracted. For greater methodological detail see Meulenbroek (2006). One way to monitor the long-wavelength drift is to compare the composite-spread time-depth function with that obtained by averaging time-depth functions computed from shorter reversed spreads. For the data considered here, the comparison indicates that long-wavelength errors are not serious.

The composite-spread approach also requires some logistical adjustment in areas where picks are poor. Because each adjacent shot point shares at least one common receiver station for the PPP picks, the compositing process has produced a single, reversed refraction spread for the PPP data (Figure 9). This is not the case for the PPS data (Figure 10). This is because there are zones where PPS refraction data could not be picked (Figure 6, Stations 235–260). In these areas, there may be no common receiver locations between adjacent picked shots such that time shifts cannot be estimated. This results in discontinuities seen on both the forward and reverse composite curves of Figures 8 and 10.

Time-depth analysis

We have performed reciprocal analysis on Figures 9 and 10 to calculate time-depths and velocity-functions. The analysis of the PPS refraction curves is somewhat more challenging than for PPP because of the lack of reversed data between Stations 235 and 270. We have generated two separate time-depth curves in areas where reversed refraction data are available. We have then combined these two curves together using a delay-time curve. As discussed in Hearn and Meulenbroek (2011), the delay-time is consistent with the time-depth for the case of a source buried in the refractor.

Inspection of Figure 10 shows that the main useable reversed refraction spread extends between Stations 100 and 235. Note that to perform reversed-spread refraction analysis over this range, we have regenerated the reverse curve referenced to a shot-point at 236.5.

A similar approach has been taken for the short reversed spread between Stations 270 and 300. In the zone where only single sided data are available (235–270) the delay-time approach has been used, modified to allow for laterally varying refractor velocity (equation 25, Hearn and Meulenbroek, 2011).

Figure 11 shows the final PPP and PPS time-depth curves for the example dataset. Note that the PPS time-depth curve has a greater amplitude and greater variability than the PPP time-depth.

Velocity analysis

Figure 12 shows the velocity function (equation 9, Hearn and Meulenbroek, 2011) derived from the PPP (black) and PPS (red) data. Again the PPS data exhibit more scatter. Because the wave-type in the refractor is the same for both PPP and PPS waves, we would expect that the slopes of the velocity functions (the reciprocal of which gives the refractor velocity, V_{2P}) would be the same. As Figure 12 shows, this is broadly the case. As noted earlier, this property can be used to confirm the validity of the converted-wave refraction picks.

Figure 13 shows the estimated refractor velocity (V_{2P}) obtained via running slope analysis of Figure 12. There is some instability in the PPS velocity function, which causes the anomalous V_{2P} variations around Station 200. With reference to Figure 6, this can be explained by the reduced number of picks in this area. When these picks are averaged at each receiver station, there is more variability, hence velocity artefacts are

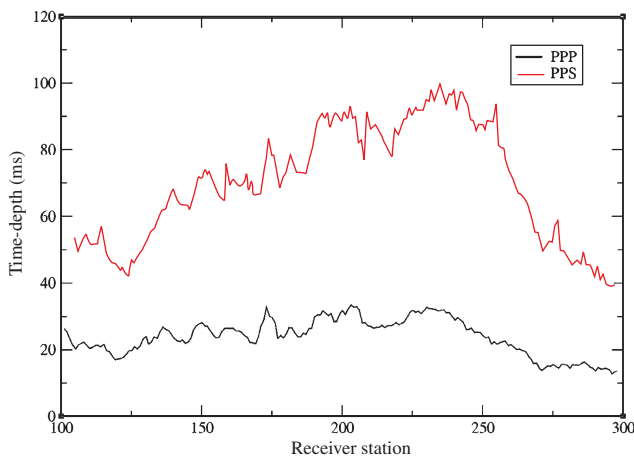


Fig. 11. PPP (black) and PPS (red) time-depth curves. The PPP curve has been constructed using a single reversed spread covering the whole line. The PPS curve has been constructed using two reversed spreads (Stations 100–235, 270–300). These two time-depth sections have been spliced using the delay-time algorithm (Stations 236–270).

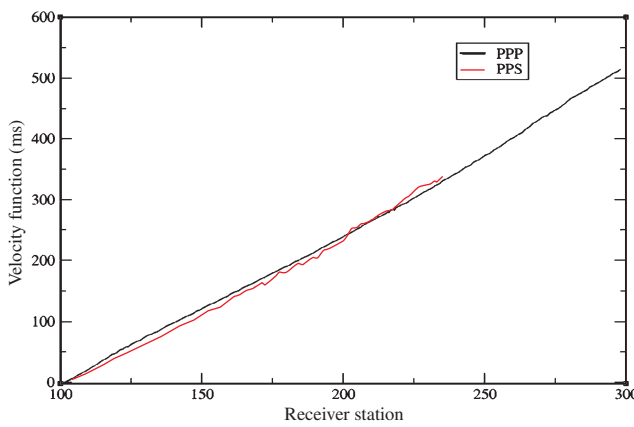


Fig. 12. Refractor velocity functions derived from PPP (black) and PPS (red) refraction data. The PPS velocity function was not calculated at the high end of the line because good quality reversed PPS refractions were not available.

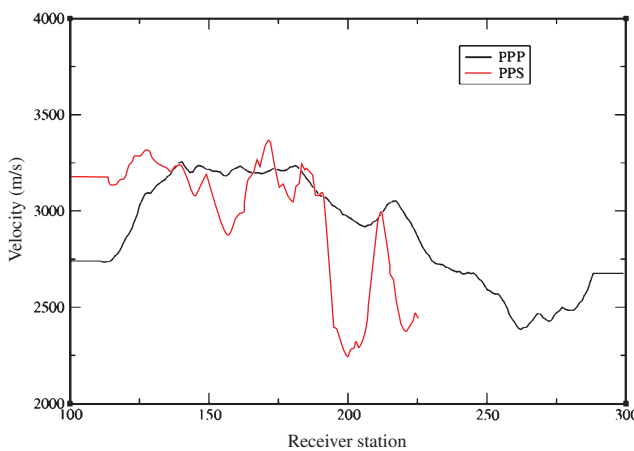


Fig. 13. V_{2P} estimated from PPP and PPS velocity functions in Figure 11. We have utilised a line of best fit within a running window of length 21 receiver stations. The inverse slope of the fitted line provides the velocity estimate for the station at the centre of the window. The anomalous velocities near Station 200 result from inaccuracy in the velocity function, arising from a lack of PPS picks.

created. In later processing stages that require knowledge of V_{2P} , we have used values derived from the PPP data, which are generally of higher quality.

Modelling of near-surface V_P/V_S ratio

The PPP and PPS time-depths (t_{GP} and t_{GS}) presented in Figure 11 are derived objectively from field refraction observations. As outlined in Hearn and Meulenbroek (2011), the ratio of these time-depths (γ^*) can be tuned to provide an improved estimate of near-surface V_P/V_S velocity ratio (γ) which is of geotechnical interest. Note that this technique implicitly assumes that the PPP and PPS refractions are generated by the same interface (or at least by interfaces at approximately the same depth).

For the dynamite dataset being analysed here, we have knowledge of V_{1P} and V_{2P} at all receiver stations. Hence the tuning algorithm makes use of V_{2P} as well as V_{1P} and γ^* at all receiver stations. Figure 14 shows the required adjustment from γ^* to γ , obtained from modelling over all practical values of V_{1P} , V_{1S} and V_{2P} .

The black line in Figure 15 shows our calculated time-depth ratio, γ^* . This curve is then tuned, using Figure 14, yielding an estimate of γ in the weathering layer (red). As noted above, knowledge of near-surface γ is of geotechnical interest. The alternate y-axis on Figure 15 shows the related parameter, dynamic Poisson's ratio (e.g. Gretener, 2003), which, in the

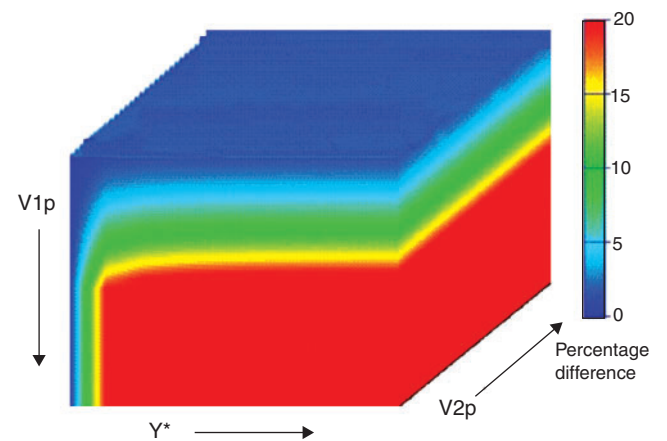


Fig. 14. Tuning volume for the case where both V_{1P} and V_{2P} are known. The volume plots the percentage difference between γ and γ^* . The range of values for the axes are $800\text{ m/s} < V_{1P} < 3000\text{ m/s}$, $1 < \gamma^* < 10$, $2500\text{ m/s} < V_{2P} < 3200\text{ m/s}$. Note that the tuning factor is independent of refractor depth.

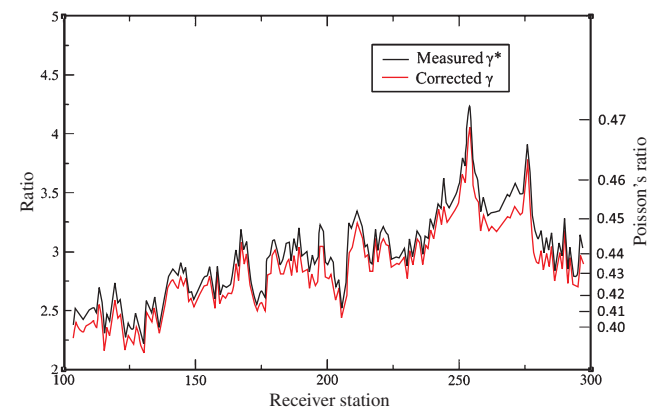


Fig. 15. Left axis: Measured γ^* (black) and estimated γ (red) calculated using the time-depth ratio tuning method. Right axis: Dynamic Poisson's ratio, corresponding to the velocity ratio (γ) on left axis.

context of petrophysics, can be used as an indicator of rock strength and changes in lithology. A lower Poisson's ratio is generally interpreted to be a stronger material. Of interest, note that the higher values of Poisson's ratio towards the right of the line (Receivers 230–280) would be consistent with fractured rocks and/or faulting. This may help to explain the reduced quality of PPS refractions in this area. We note that this is also the area in which the delay-time algorithm has necessarily been used. It is possible that the derived time-depths are therefore less accurate in this area. However, we believe such errors have been minimised by a delay-time formulation which allows for lateral variations in V_{2P} (equation 25, Hearn and Meulenbroek, 2011).

The near-surface γ values derived in this study ($\gamma = 2.5\text{--}4$) are greater than those derived at depth ($\gamma = 1.5\text{--}2.5$) using converted-wave reflection (Velseis, 2007). The geology in this area consists of interbedded sandstones and shales, with lateral heterogeneity expected both in the near-surface and at depth. Typical values of γ in the literature for these rocks (e.g. Domenico, 1984) are consistent with γ values derived at depth in Velseis (2007). It is reasonable that γ values are higher in the weathering layer. The material is likely to be less consolidated, and the weathering process is likely to increase porosity. This result is consistent with Tatham (1982) who has noted this general trend of increasing γ with increasing porosity for published sandstone velocities.

Derivation of S-wave receiver statics

As described above, a relatively objective estimate of surface layer γ (V_P/V_S) can be obtained from the observed PPP and PPS time-depth functions. For the dynamite dataset analysed here, a detailed V_{1P} function is also available from uphole times. Hence the V_{1S} function can be calculated. (More generally, for a surface source only an approximate V_{1P} function would be available, and this would be used, with γ , to derive an approximate V_{1S} function.)

Using the time-depth and V_{2P} derived from PPP data, the depth to the base of weathering can be calculated. The final S-wave weathering correction is obtained by stripping off the weathered layer (velocity = V_{1S}) and replacing it with the sub-weathering layer (velocity = V_{2S}). In the absence of detailed knowledge of variations in sub-weathering S-wave velocity, we have assumed a constant γ value of 2.0 in the refractor. This nominal value is based on converted-wave reflection results from Velseis (2007). Note that this parameter has much less influence on statics than γ in the weathering layer.

Figure 16 shows the final S-wave receiver weathering static corrections for the ACARP #3 data compared with the corresponding P-wave receiver corrections. Note that the S-wave receiver static corrections have higher amplitude than the corresponding P-wave statics. The PPS curve also exhibits greater variability, particularly station-to-station (short wavelength) variability. These results have been noted in previous studies into S-wave receiver statics (e.g. Garotta et al., 2004).

We now examine the application of these statics to our converted-wave reflection data. The images considered below are constant- γ common-conversion-point (CCP) stacks. These are analogous to constant-velocity CMP stacks in P-wave processing. The results are presented at this stage of processing because we wish to illustrate the improvements obtained with only the application of converted-wave static corrections. Positive and negative offset stacks are shown separately because of observed diodic illumination (e.g. Thomsen, 1999; Li et al., 2001). It is believed that the cause of diodic illumination in this area is a very clean sandstone channel through which the positive offset S-wave is propagating but the

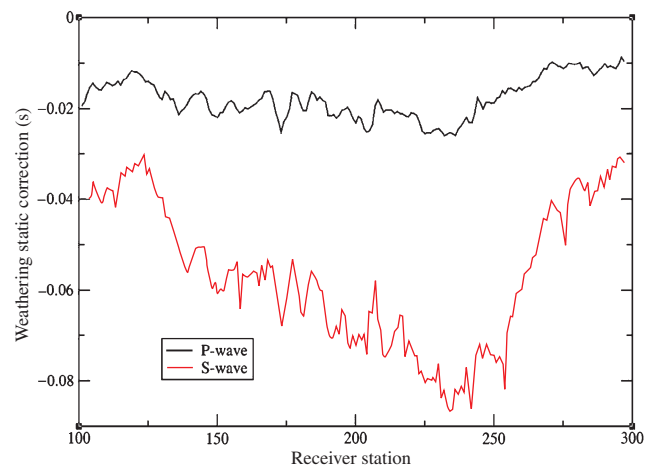


Fig. 16. Comparison of final P- and S-wave weathering static corrections. The P-wave corrections (black) are derived from conventional PPP refraction data. The S-wave corrections (red) exploit both PPP and PPS refractions, as described in the text.

negative offset S-wave is not (Velseis, 2007). Both the positive and negative offset sections are stacked using the same γ values.

Figure 17 shows a negative-offset CCP stack with P-wave source statics applied, but with no S-wave receiver static corrections. The target PS reflector is indicated. Arrows indicate an apparent anticline and a discontinuity in the reflector. In Figure 18, the S-wave receiver static corrections from Figure 16 have been applied. The apparent structure has been removed and the discontinuity has been resolved. By analogy with conventional P-wave statics workflow, we apply a converted-wave residual static correction (Velseis, 2007) after the application of converted-wave refraction statics (Figure 19), to remove any residual static errors that may still be present. A further subtle improvement is achieved.

Figures 20–22 show the corresponding positive offset CCP stacks with no S-wave receiver statics, converted-wave receiver statics, and converted-wave receiver statics followed by converted-wave residual statics respectively. Comparison between Figures 20 and 21 shows a general flattening of the apparent structures seen in the target reflector. Towards the high CCP numbers however, the application of refraction statics appears to degrade the continuity of the target reflector with

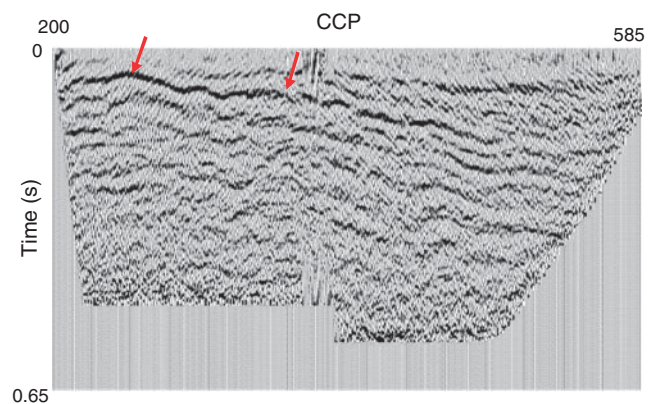


Fig. 17. Negative offset common-conversion-point (CCP) stack with no S-wave receiver static corrections applied. The target PS refraction event is indicated. Note the apparent anticline and the discontinuity in the target event. In this figure and the following seismic sections, the horizontal extent is approximately the same as for the preceding refraction analyses. The CCP on the sections relates to Receiver Station by a factor of two.

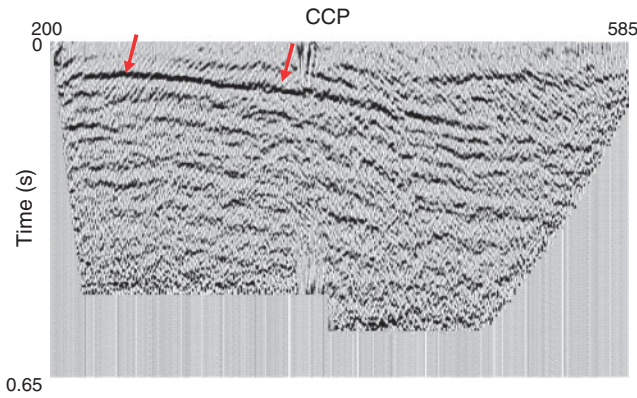


Fig. 18. Negative offset common-conversion-point (CCP) stack with S-wave receiver static corrections applied. Compare with Figure 17. The apparent structure in the PS reflector has been removed and the continuity has been significantly improved.

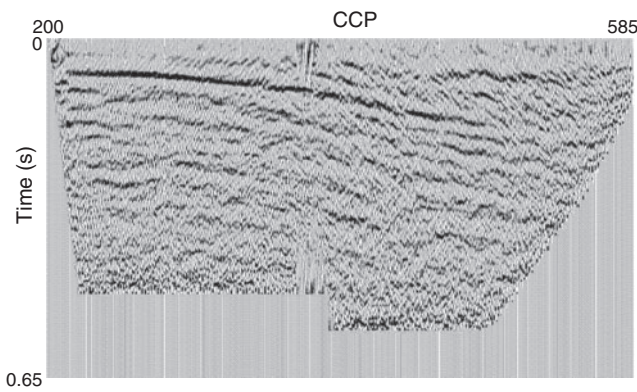


Fig. 19. Negative offset common-conversion-point (CCP) stack with S-wave receiver static corrections applied, followed by converted-wave residual statics. This has provided a further subtle improvement to the stack in Figure 18.

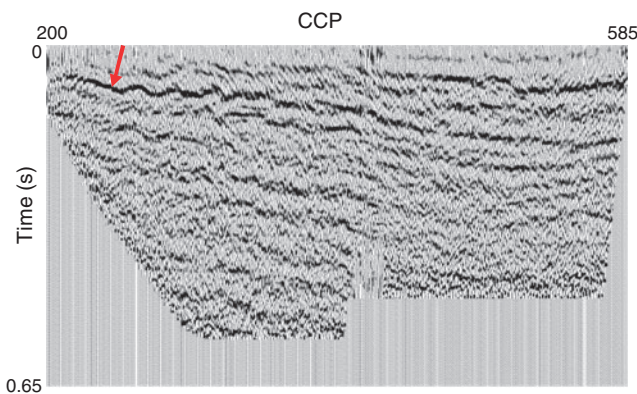


Fig. 20. Positive offset common-conversion-point (CCP) stack with P-wave source static corrections, but no S-wave receiver corrections, applied. The target reflector is indicated.

respect to the no-statics solution. This suggests that the derived statics solution is not correct in this region. Recall that the PPS refractions in this area were difficult to identify. Clearly, if PPS arrivals are of poor quality, the derived S-wave statics need to be treated with caution. Fortunately, in this case, the subsequent application of residual statics (Figure 22) has largely recovered

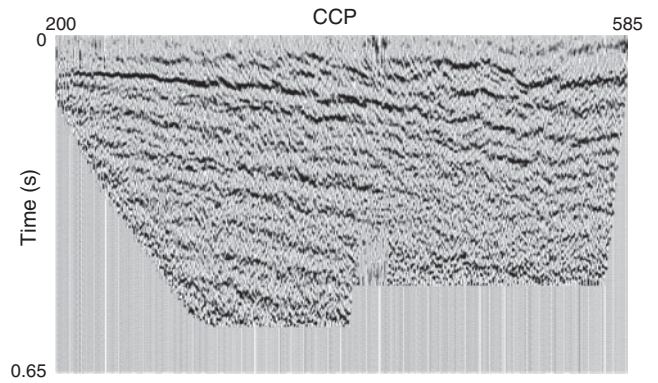


Fig. 21. Positive offset common-conversion-point (CCP) stack with converted-wave refraction static corrections applied. Compare with Figure 20.

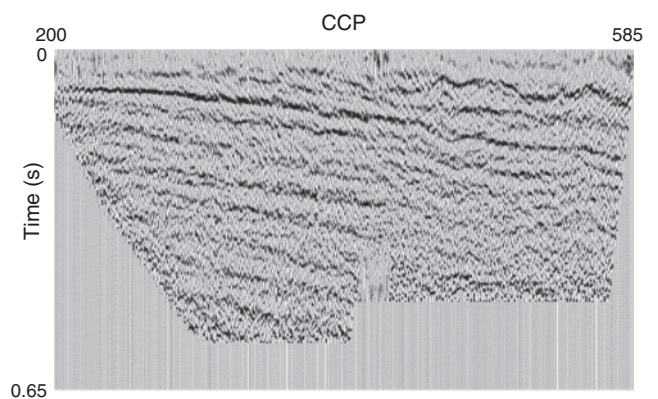


Fig. 22. Positive offset common-conversion-point (CCP) stack with converted-wave refraction static corrections applied followed by converted-wave residual static corrections. Compare with Figure 21.

the degradation introduced at the high CCP numbers. At the low CCP numbers, the application of converted-wave residual statics has, again, provided a subtle improvement to the previous stack.

Conclusions

We have demonstrated a practical approach to estimating S-wave receiver statics via reciprocal analysis of converted (PPS) refractions. The main thrust of this work is to provide receiver statics for converted (PS) reflection data. For the example presented here, the best results overall have been obtained when the deterministic refraction method was followed by an appropriate statistical residual method. This is analogous to the workflow commonly used in conventional P-wave statics processing.

There are several practical considerations when using this method, from both an acquisition and processing standpoint. Examination of several datasets indicates that geophones with a low resonant frequency (e.g. 10–15 Hz) are required if PPS refractions are to be easily identified. MEMs receivers may provide an attractive alternative because of their good low-frequency response. Several processing considerations for this technique were derived in a companion paper (Hearn and Meulenbroek, 2011). The final reflection sections show that the derived refraction method is a viable approach to solving the problem of S-wave receiver statics.

Although this work has been primarily directed towards derivation of S-wave statics, an interesting auxiliary output is also available. Based on theoretical modelling, the S-to-P time-

depth ratios can be tuned to provide P-to-S velocity ratios, even in cases where the surface V_P and V_S cannot be individually determined (e.g. when a surface source is used). This leads to useful associated parameters such as dynamic Poisson's ratio. Used in the correct context, this has interesting implications for lithological and rock-strength analysis in mining, environmental and geotechnical investigations.

In this paper, we have analysed PPS refractions from a dynamite source buried in the refractor. The analysis for a surface source is only slightly different. The reciprocal analysis is easier to perform since the true shot-to-shot time is directly measurable from the data. The surface layer γ can still be estimated using the observed S-to-P time-depth ratio. As in conventional Vibroseis refraction statics, the weathering velocity V_{1P} is likely to be more poorly defined than for dynamite surveys. If V_{1P} is completely unknown, then applying a 5% reduction in the derived time-depth ratio (γ^*) would be appropriate for typical near-surface geologies. This corresponds to a nominal weathering velocity of 1000 ms^{-1} (see Figure 14).

The concepts presented here are derived largely from a single case study, where converted refractions were reasonably easy to identify. Examination of several other datasets suggests that this is not always the case. Future research is required into the factors which lead to a well defined PPS refraction. These factors may be geological (e.g. lithological contrasts, anelastic attenuation, fracturing) and geophysical (e.g. source type, geophone resonant frequency, recording filters). Full assessment of these factors will require examination of multiple datasets, and viscoelastic modelling. A methodological goal is to explore more sophisticated preprocessing techniques to enable better identification of the PPS refraction.

Acknowledgements

This work draws on Alan Meulenbroek's Honours (Meulenbroek, 2006) and postgraduate research at the University of Queensland, and has been supported by the ASEG Research Foundation. The real data presented in this paper have been made available with the support of the Australian Coal Association Research Program (ACARP). Our data processing code makes use of the framework provided by Seismic UN*X from CWP, Colorado School of Mines. We thank Derecke Palmer and two anonymous reviewers of this manuscript.

References

- Brown, R. J., Stewart, R. R., Gasier, J. E., and Lawton, D. C., 2002, A proposed polarity standard for multicomponent seismic data: *Geophysics*, **67**, 1028–1037. doi:10.1190/1.1500363
- Cary, P. W., and Eaton, D. W. S., 1993, A simple method for resolving large converted-wave (P-SV) statics: *Geophysics*, **58**, 429–433. doi:10.1190/1.1443426
- Domenico, S. N., 1984, Rock lithology and porosity determination from shear and compressional wave velocity: *Geophysics*, **49**, 1188–1195. doi:10.1190/1.1441748
- Gardner, L. W., 1939, An areal plan of mapping subsurface structure by refraction shooting: *Geophysics*, **4**, 247–259. doi:10.1190/1.1440501
- Garotta, R., Granger, P. Y., and Gresillaud, A., 2004, About compressional, converted-mode, and shear statics: *The Leading Edge*, **23**, 526–532. doi:10.1190/1.1766242
- Gretener, P., 2003, Summary of the Poisson's Ratio debate 1990–2003: *Recorder*, **28**, 44–45.
- Hagedoorn, J. G., 1959, The plus-minus method of interpreting seismic refraction lines: *Geophysical Prospecting*, **6**, 285–314.
- Hagiwara, T., and Omote, S., 1939, Land creep at Mt Tyausu – Yama (Determination of slip plane by seismic prospecting): *Tokyo University Earthquake Research Institute Bulletin*, **17**, 118–137.
- Hawkins, L. V., 1961, The reciprocal method of routine shallow seismic refraction investigations: *Geophysics*, **26**, 806–819. doi:10.1190/1.1438961
- Hearn, S., and Meulenbroek, A., 2011, Ray-path concepts for converted-wave refraction: *Exploration Geophysics*, **42**, 139–146. doi:10.1071/EG10030
- Hearn, S., and Stanley, M., 1983, High resolution weathering corrections from breaks of reflection records: ASEG 3rd Biennial Conference, Expanded Abstracts, 53–54.
- Houston, L. M., Rice, J. A., and Cameron, D. S., 1989, Method for shear-wave statics corrections using converted wave refractions: *SEG Technical Program. Expanded Abstracts*, **8**, 1298–1301. doi:10.1190/1.1889506
- Li, X. Y., Dai, H., Meuller, M., and Barkved, O., 2001, Compensating for the effects of gas clouds on C-wave imaging: a case study from Valhall: *The Leading Edge*, **20**, 1022–1028. doi:10.1190/1.1487307
- Meulenbroek, A., 2006, A converted-wave refraction statics technique with applications to near-surface characterisation: Honours thesis, University of Queensland.
- Schafer, A. W., 1991, The determination of converted-wave statics using P refractions together with SV refractions: *SEG Technical Program. Expanded Abstracts*, **10**, 1413–1415. doi:10.1190/1.1889086
- Tatham, R. H., 1982, V_P/V_S and lithology: *Geophysics*, **47**, 336–344. doi:10.1190/1.1441339
- Thomsen, L., 1999, Converted-wave reflection seismology over inhomogeneous, anisotropic media: *Geophysics*, **64**, 678–690. doi:10.1190/1.1444577
- Vasil'ev, Y. I., 1957, Study of alternating refracted waves in seismic prospecting: *Izvestiya Akademii Nauk SSSR Seriya Geofizicheskaya Bulletin of the Academy of Sciences of the U.S.S.R. Geophysics Series*, **3**, 301–318.
- Velseis, 2007, Integrated P-wave/PS-wave seismic imaging for improved geological characterisation of coal environments. Final Report: Australian Coal Association Research Program (ACARP) project C13029.

Manuscript received 27 October 2010; accepted 26 May 2011.